

Solvent-induced polarization dynamics and coherent two-dimensional spectroscopy: Dissipaton equation of motion approach



Hou-Dao Zhang^a, Qin Qiao^b, Rui-Xue Xu^c, Yijing Yan^{b,*}

^a Department of Chemical Physics, University of Science and Technology of China, Hefei 230026, China

^b Hefei National Laboratory for Physical Sciences at the Microscale and Collaborative Innovation Center of Chemistry for Energy Materials (iChEM), University of Science and Technology of China, Hefei 230026, China

^c Hefei National Laboratory for Physical Sciences at the Microscale and Synergetic Innovation Center of Quantum Information and Quantum Physics, University of Science and Technology of China, Hefei 230026, China

ARTICLE INFO

Article history:

Available online 16 July 2016

Keywords:

Hybrid bath dynamics
Dissipation equation of motion
Generalized Wick's theorem
Multidimensional coherent spectroscopy
Fano entanglement spectroscopy

ABSTRACT

This work exploits the **dissipaton equation of motion** (DEOM) approach to study the solvent-induced non-Condon polarization dynamics and its two-dimensional coherent spectroscopy for model excitonic systems. DEOM is a second quantization generation of the celebrated hierarchical equations of motion theory, with the capability of accurate evaluation for both reduced system and hybrid bath dynamics. The underlying dissipaton algebra includes the generalized Wick's theorem and DEOM-space techniques for hybrid bath dynamics. Methods discussed also involve an efficient derivative–resum level truncation scheme that preserves the prescription invariance, and the mixed Heisenberg–Schrödinger picture approach for efficient simulation of nonlinear response functions. Our model simulations show clearly the correlated system-and-bath interference and the resulting Fano entanglement spectroscopy profiles.

© 2016 Elsevier B.V. All rights reserved.

1. Introduction

Quantum dissipation plays a pivotal role in many research fields, such as the chemical reactions [1], quantum transports [2], and **excitation energy transfer** [3]. As an exact and non-perturbative method, the hierarchical-equations-of-motion (HEOM) theory has been used extensively in studying various quantum dissipation and quantum transport systems [4–15]. On the other hand, multidimensional coherent spectroscopy is a powerful experimental tool in monitoring intra- and intermolecular interactions, and the underlying quantum transfer and dissipation processes [16–18]. It has revealed the long lived electronic and vibrational quantum coherence in light harvesting pigment–protein complexes [19–25]. In these nanostructured systems, the interactions within the system and between system and environment have comparable strength, while the timescale of system dynamics overlaps with that of the environment fluctuations [3]. The above structural and dynamical characteristics, as well as the nonlinear nature of ultrafast multidimensional spectroscopy, call for a non-perturbative and non-Markovian treatment, based on such as the exact HEOM approach [26–33]. However, HEOM focuses primarily only on the reduced system, despite of its involving a

vast number of auxiliary density operators that are purely mathematical quantities [4–7,11–14].

In this paper, we exploit the newly developed dissipaton equation of motion (DEOM) theory [34–37], to study the solvent-induced non-Condon polarization dynamics and related two-dimensional coherent spectroscopy. To our best knowledge, DEOM is by far the only theory that can treat both reduced system and hybrid bath dynamics. The new theory provides a quasi-particle picture for the influence of bath. Dynamical variables in DEOM are called **dissipaton density operators** (DDOs), which are no longer mathematical auxiliaries, but physically related to the reduced description of multi-dissipaton configurations. Not only it is about how the DDOs evolve in time, the DEOM theory includes also the underlying dissipaton algebra [34–37], especially the generalized Wick's theorem. This enables us to investigate the hybrid bath dynamics that is experimentally measurable, such as Fano interferences [35] and quantum transport current noise spectrum [36].

We also discuss the issue of hierarchy level truncation, from not only the numerical aspect, but also the fundamental requirement of prescription invariance. In other words, **the truncation approximation made in Schrödinger picture** should sufficiently lead to the Heisenberg picture correspondence without further approximation [38]. This requirement is practically important in the mixed Heisenberg–Schrödinger dynamics for efficient evaluation of nonlinear correlation functions. The DEOM-space extension of

* Corresponding author.

E-mail address: yanyj@ustc.edu.cn (Y.J. Yan).

dynamical variables, the Heisenberg equations of motion and the initial values are all determined via the dissipaton algebra, and demonstrated with the third-order optical correlation functions for excitonic systems with non-Condon transition dipoles.

This paper is organized as follows. In Section 2, after describing the model excitonic system, we construct the DEOM formalism, together with the detailed derivations and the underlying dissipaton algebra. In Section 3, we present the DEOM-space linear algebra, the mixed Heisenberg–Schrödinger dynamics scheme, and the block-matrix method for efficient evaluation of nonlinear response functions. We also highlight the efficient derivative–resum truncation scheme that preserves the prescription invariance. In Section 4, we simulate the solvent-induced non-Condon polarization dynamics and the two-dimensional coherent spectroscopies for model excitonic monomer and dimer systems. Our simulations show clearly the correlated system-and-bath dynamics and the resulting Fano entanglement spectroscopy profiles. In Section 5, we conclude this work.

2. DEOM theory

2.1. Prelude

Consider a multi-chromophore system embedded in a polarizable environment, in which the **bath-induced non-Condon optical transition occurs**. The excitonic system Hamiltonian is

$$H_S = \sum_a \epsilon_a \hat{B}_a^\dagger \hat{B}_a + \sum_{a \neq b} V_{ab} \hat{B}_a^\dagger \hat{B}_b + \sum_{a > b} U_{ab} \hat{B}_a^\dagger \hat{B}_b^\dagger \hat{B}_a \hat{B}_b. \quad (1)$$

Here, \hat{B}_a^\dagger (\hat{B}_a) is the excitonic creation (annihilation) operator for the specified local chromophore with energy ϵ_a . The parameters V_{ab} and U_{ab} represent the inter-chromophore coupling and the double-excitation energy shift, respectively. The system-bath coupling assumes the form,

$$H_{SB} = \sum_a \hat{Q}_a \hat{F}_a, \quad \text{where} \quad \hat{Q}_a = \hat{B}_a^\dagger \hat{B}_a, \quad (2)$$

and $\hat{F}_a = \sum_j c_{aj} \hat{x}_j$, with $\{\hat{x}_j\}$ denoting the harmonic bath coordinates. The matter-field interaction is given by

$$H_{\text{mat-fld}}(t) = - \sum_a \mu_a(\hat{\mathbf{X}}_a) \hat{D}_a \mathcal{E}(t), \quad (3)$$

with $\hat{D}_a = \hat{B}_a^\dagger + \hat{B}_a$ being the electronic transition operator and $\mu_a(\hat{\mathbf{X}}_a)$ the electronic transition element. The latter depends in general on the nuclear coordinates $\hat{\mathbf{X}}_a$ of the total system-and-bath composite space. In this work, we consider the simplest bath-induced non-Condon transition case, modeled by

$$\mu_a(\hat{\mathbf{X}}_a) = \mu_a + v_a \hat{F}_a. \quad (4)$$

The total composite Hamiltonian in the presence of external field drive can now be recast as

$$H_T(t) = H(t) + h_B + \sum_a \hat{Q}_a^{\text{eff}}(t) \hat{F}_a, \quad (5)$$

where

$$H(t) = H_S - \sum_a \mu_a \hat{D}_a \mathcal{E}(t), \quad (6)$$

$$\hat{Q}_a^{\text{eff}}(t) = \hat{Q}_a - v_a \hat{D}_a \mathcal{E}(t).$$

For later use, we denote $\mathcal{L}(t)\hat{O} \equiv [H(t), \hat{O}]$, for the system Liouvillian. Throughout this paper, we set $\hbar = 1$ and $\beta = 1/(k_B T)$, with k_B and T being the Boltzmann constant and temperature, respectively. Set hereafter the time variable $t > 0$, unless further specified.

In the h_B -interaction picture, $\hat{F}_a(t) \equiv e^{ih_B t} \hat{F}_a e^{-ih_B t}$, which is a Gaussian stochastic bath variable in present study. Its influence on the reduced system is entirely described by the following correlation functions in the bare-bath ensemble,

$$\langle \hat{F}_a(t) \hat{F}_b(0) \rangle_B = \frac{1}{\pi} \int_{-\infty}^{\infty} d\omega \frac{e^{-i\omega t} J_{ab}(\omega)}{1 - e^{-\beta\omega}} = \sum_{k=1}^K \eta_{abk} e^{-\gamma_k t}. \quad (7)$$

The first identity is the **fluctuation-dissipation theorem** [39,40], which links the bath correlation and the spectral density $J_{ab}(\omega) = \frac{\pi}{2} \sum_j c_{aj} c_{bj} \delta(\omega - \omega_j)$. The second identity, which would be exact when $K \rightarrow \infty$, are obtained via certain sum-over-pole scheme on $J_{ab}(\omega)$ and the Bose function $1/(1 - e^{-\beta\omega})$, followed by the Cauchy contour integral [41,42]. In general, $\{\eta_{abk}\}$ and $\{\gamma_k\}$ are complex. The time-reversal counterpart to Eq. (7) is

$$\langle \hat{F}_b(0) \hat{F}_a(t) \rangle_B = \langle \hat{F}_a(t) \hat{F}_b(0) \rangle_B^* = \sum_{k=1}^K \eta_{ab\bar{k}}^* e^{-\gamma_k^* t}. \quad (8)$$

The second identity, where the associate index \bar{k} goes with $\gamma_k^* = \gamma_{\bar{k}}$, reflects the fact that γ_k and γ_k^* must both appear if they are complex. Apparently, $\bar{k} = k$ for a real γ_k .

2.2. DEOM formalism

The DEOM theory is based on the quasi-particle description of the hybrid bath [34]. The hybridization bath operator \hat{F}_a is decomposed into a set of statistically independent dissipatons; i.e.,

$$\hat{F}_a = \sum_{k=1}^K \hat{f}_{ak}, \quad (9)$$

with

$$\begin{aligned} \langle \hat{f}_{ak}(t) \hat{f}_{bj}(0) \rangle_B &= \delta_{kj} \eta_{abk} e^{-\gamma_k t}, \\ \langle \hat{f}_{bj}(0) \hat{f}_{ak}(t) \rangle_B &= \delta_{kj} \eta_{ab\bar{k}}^* e^{-\gamma_k^* t}. \end{aligned} \quad (10)$$

The bath correlations, Eqs. (7) and (8), are both recovered. Thus, the Gaussian bath influence on system is faithfully preserved. Note the dissipaton correlation functions along the forward and backward pathways are of the same exponents. This feature highlights the generalized diffusion nature of dissipatons, see Eq. (17) for further elaboration.

Dynamical variables of DEOM are the so-called *dissipaton density operators* (DDOs), defined as

$$\rho_{\mathbf{n}}^{(n)}(t) \equiv \text{tr}_B \left[\left(\prod_{ak} \hat{f}_{ak}^{n_{ak}} \right)^\circ \rho_T(t) \right]. \quad (11)$$

Here, $\rho_T(t)$ is the total system-and-bath composite density operator, and tr_B denotes the trace over bath degrees of freedom. The product of dissipaton operators inside the circled parentheses is *irreducible*. The notation here follows (c-number) $^\circ = 0$, and bosonic dissipatons are permutable, $(\hat{f}_{ak} \hat{f}_{bj})^\circ = (\hat{f}_{bj} \hat{f}_{ak})^\circ$. In Eq. (11), $\mathbf{n} \equiv \{n_{ak}\}$ and $n \equiv \sum_{ak} n_{ak}$, with n_{ak} being the participation number of individual dissipaton. Apparently, $\rho^{(0)} = \text{tr}_B \rho_T = \rho_S$ is the reduced system density operator. Those $\{\rho_{\mathbf{n}}^{(n>0)}\}$ specify n -body dissipaton configurations, rather than the mathematical auxiliaries as those in HEOM [6,7,11–13]. Denote also the adjacent upper and lower level neighbors, $\rho_{\mathbf{n}_{ak}^+}^{(n+1)}$ and $\rho_{\mathbf{n}_{ak}^-}^{(n-1)}$, with the associated index \mathbf{n}_{ak}^\pm differing from \mathbf{n} by $n_{ak} \pm 1$, at the specified dissipaton.

The DEOM formalism, with the bath-induced non-Condon transition in study [cf. Eq. (5)], can be derived via the established dissipaton algebra [34–37]. The detailed derivation is presented in Section 2.3. The final results read

$$\dot{\rho}_{\mathbf{n}}^{(n)} = - \left[i\mathcal{L}(t) + \sum_{ak} n_{ak} \gamma_k \right] \rho_{\mathbf{n}}^{(n)} - i \sum_{ak} \mathcal{A}_a(t) \rho_{\mathbf{n}_{ak}^+}^{(n+1)} - i \sum_{ak} n_{ak} \mathcal{C}_{ak}(t) \rho_{\mathbf{n}_{ak}^+}^{(n-1)}, \quad (12)$$

where [see $\hat{Q}_a^{\text{eff}}(t)$ in Eq. (6)]

$$\mathcal{A}_a(t) \hat{O} \equiv [\hat{Q}_a^{\text{eff}}(t), \hat{O}], \quad (13)$$

$$\mathcal{C}_{ak}(t) \hat{O} \equiv \sum_b [\eta_{abk} \hat{Q}_b^{\text{eff}}(t) \hat{O} - \eta_{abk}^* \hat{O} \hat{Q}_b^{\text{eff}}(t)].$$

In absence of bath-induced non-Condon transition, $v_a = 0$ and $\hat{Q}_a^{\text{eff}}(t) = \hat{Q}_a$, Eq. (12) recovers the celebrated HEOM formalism [6,7,11–13], constructed originally on the basis of Feynman-Vernon influence functional path integral expression [43]. However, the dynamical variables in DEOM are the physically meaningful DDOs [cf. Eq. (11)], rather than mathematical auxiliaries in HEOM. The DDOs and the underlying dissipation algebra are responsible for hybrid bath dynamics in DEOM.

DEOM (12) involves infinite hierarchy. To truncate the formalism at certain level L , we adopt the derivative-resum scheme [37,38,44],

$$\dot{\rho}_{\mathbf{n}_{bj}^+}^{(L+1)} \approx -i \sum_{ak} \mathcal{A}_a(t) \rho_{\mathbf{n}_{bj,ak}^+}^{(L+2)}. \quad (14)$$

This is equivalent to [37,38]

$$\rho_{\mathbf{n}_{bj}^+}^{(L+1)} = \frac{-i}{i\mathcal{L}(t) + \sum_{ak} (n_{ak} + \delta_{ak,bj}) \gamma_k} \times \sum_{ak} (n_{ak} + \delta_{ak,bj}) \mathcal{C}_{ak}(t) \rho_{\mathbf{n}_{bj,ak}^+}^{(L)}. \quad (15)$$

Here, $\delta_{ak,bj} = \delta_{ab} \delta_{kj}$ and $\mathbf{n}_{bj,ak}^{\pm}$ differs from \mathbf{n} by $n_{bj} + 1$ and $n_{ak} \pm 1$. The derivative-resum is the best choice among all existing truncation schemes we tested by far. It not only is numerically efficient, but also preserves the prescription invariance. While Eq. (15) is used to close the Schrödinger picture DEOM (12), the equivalent Eq. (14) will map to the terminal equation for the Heisenberg picture DEOM, as to be discussed in Section 3. A truncation scheme similar to Eq. (15), but involving further a local classical treatment, has been proposed by Tanimura and Wolynes [45] and adopted in many numerical studies [7,9,10,26–29,46]. See Ref. [38] for the detailed comparisons.

2.3. Derivation of DEOM and comments

The DEOM (12) is derived by applying the Liouville–von Neumann equation,

$$\dot{\rho}_{\text{T}} = -i \left[H(t) + h_{\text{B}} + \sum_a \hat{Q}_a^{\text{eff}}(t) \hat{F}_a, \rho_{\text{T}} \right], \quad (16)$$

for the total composite density operator in Eq. (11), with the hybrid bath \hat{F}_a being in the dissipaton decomposition form of Eq. (9). Apparently, the field-dressed system Hamiltonian, $H(t)$, gives rise to the $\mathcal{L}(t)$ -term in Eq. (12). The derivation of other terms involves generalized diffusion equation and generalized Wick's theorem for dissipatons. The details are as follows.

2.3.1. Generalized diffusion equation

Consider the effect of h_{B} -commutator action on the DDOs, Eq. (11). Each dissipaton \hat{f}_{ak} is characterized by a single exponent, as specified in Eq. (10), for its correlation functions along both forward and backward paths. This property leads to (setting $\partial_t \equiv \frac{\partial}{\partial t}$)

$$\text{tr}_{\text{B}} \left[\left(\partial_t \hat{f}_{ak} \right)_{\text{B}} \rho_{\text{T}}(t) \right] = -\gamma_k \text{tr}_{\text{B}} \left[\hat{f}_{ak} \rho_{\text{T}}(t) \right]. \quad (17)$$

This is the generalized diffusion equation for dissipatons [34–37]. The complex γ_k would occur when an underdamped Brownian oscillator is in consideration. Eq. (17) is used together with the Heisenberg equation of motion in the bare-bath, $\left(\partial_t \hat{f}_{ak} \right)_{\text{B}} = -i [\hat{f}_{ak}, h_{\text{B}}]$, for the evaluation of the effect of commutator action of h_{B} on the DDOs, as follows.

$$\begin{aligned} -i \text{tr}_{\text{B}} \left\{ \left(\prod_{ak} \hat{f}_{ak}^{n_{ak}} \right)^{\circ} [h_{\text{B}}, \rho_{\text{T}}] \right\} &= -i \text{tr}_{\text{B}} \left\{ \left[\left(\prod_{ak} \hat{f}_{ak}^{n_{ak}} \right)^{\circ}, h_{\text{B}} \right] \rho_{\text{T}} \right\} \\ &= \text{tr}_{\text{B}} \left\{ \left[\frac{\partial}{\partial t} \left(\prod_{ak} \hat{f}_{ak}^{n_{ak}} \right)^{\circ} \right]_{\text{B}} \rho_{\text{T}} \right\} \\ &= - \left(\sum_{ak} n_{ak} \gamma_k \right) \text{tr}_{\text{B}} \left\{ \left(\prod_{ak} \hat{f}_{ak}^{n_{ak}} \right)^{\circ} \rho_{\text{T}} \right\} \\ &= - \left(\sum_{ak} n_{ak} \gamma_k \right) \rho_{\mathbf{n}}^{(n)}. \end{aligned} \quad (18)$$

This leads to the last term in the first parentheses of Eq. (12).

2.3.2. Generalized Wick's theorem

We now evaluate the influence of $\sum_{ak} \hat{Q}_a^{\text{eff}}(t) \hat{f}_{ak}$ on DDOs, which will lead to the last two terms in Eq. (12). Recall the definition of $\rho_{\mathbf{n}}^{(n)}$ in Eq. (11), where the dissipatons product inside $(\dots)^{\circ}$ is *irreducible*. This notation supports the generalized Wick's theorem [34–37]:

$$\text{tr}_{\text{B}} \left[\left(\prod_{ak} \hat{f}_{ak}^{n_{ak}} \right)^{\circ} \hat{f}_{bj} \rho_{\text{T}} \right] = \rho_{\mathbf{n}_{bj}^+}^{(n+1)} + \sum_{ak} n_{ak} \langle \hat{f}_{ak} \hat{f}_{bj} \rangle_{\text{B}}^> \rho_{\mathbf{n}_{ak}^+}^{(n-1)}, \quad (19)$$

and

$$\text{tr}_{\text{B}} \left[\left(\prod_{ak} \hat{f}_{ak}^{n_{ak}} \right)^{\circ} \rho_{\text{T}} \hat{f}_{bj} \right] = \rho_{\mathbf{n}_{bj}^+}^{(n+1)} + \sum_{ak} n_{ak} \langle \hat{f}_{bj} \hat{f}_{ak} \rangle_{\text{B}}^< \rho_{\mathbf{n}_{ak}^+}^{(n-1)}. \quad (20)$$

The contraction terms involve the values of dissipaton correlation functions, Eq. (10), at $t = 0+$. They are

$$\begin{aligned} \langle \hat{f}_{ak} \hat{f}_{bj} \rangle_{\text{B}}^> &\equiv \langle \hat{f}_{ak}(0+) \hat{f}_{bj} \rangle = \delta_{kj} \eta_{abk}, \\ \langle \hat{f}_{bj} \hat{f}_{ak} \rangle_{\text{B}}^< &\equiv \langle \hat{f}_{bj} \hat{f}_{ak}(0+) \rangle = \delta_{kj} \eta_{abk}^*. \end{aligned} \quad (21)$$

The generalized Wick's theorem, Eqs. (19) and (20), holds for Gaussian bath influences, regardless whether the total composite ρ_{T} is Gaussian or not. The effect of the last term of the total composite Hamiltonian (5) can now be evaluated readily as

$$\begin{aligned} \sum_{bj} \text{tr}_{\text{B}} \left\{ \left(\prod_{ak} \hat{f}_{ak}^{n_{ak}} \right)^{\circ} \left[\hat{Q}_b^{\text{eff}}(t) \hat{f}_{bj}, \rho_{\text{T}} \right] \right\} \\ = \sum_{abk} n_{ak} \left[\eta_{abk} \hat{Q}_b^{\text{eff}}(t) \rho_{\mathbf{n}_{ak}^+}^{(n-1)} - \eta_{abk}^* \rho_{\mathbf{n}_{ak}^+}^{(n-1)} \hat{Q}_b^{\text{eff}}(t) \right] \\ + \sum_{bj} \left[\hat{Q}_b^{\text{eff}}(t), \rho_{\mathbf{n}_{bj}^+}^{(n+1)} \right]. \end{aligned} \quad (22)$$

Evidently, the above expression contributes to the last two terms in Eq. (12).

3. Heisenberg picture and DEOM-space algebra

3.1. Schrödinger versus Heisenberg picture

We extend the Liouville-space algebra for isolated systems [47] to the DEOM-space for entangled system-and-bath dynamics. Without loss of generality, we consider only the time-independent case in absence of external field. The resulting DEOM formalisms in Schrödinger picture and Heisenberg picture are relevant to the evaluation of correlation functions. Let $\rho(t) \equiv \{\rho_S(t), \rho_{\mathbf{n}}^{(n>0)}(t)\}$ be the DEOM-space state vector. **The time evolution of $\rho(t)$ is the Schrödinger picture and reads**

$$\dot{\rho}(t) = -i\mathcal{L}\rho(t). \quad (23)$$

The DEOM-space dynamics generator \mathcal{L} is defined by Eq. (12) in the absence of external field. The Heisenberg picture adopts the same \mathcal{L} but for the evolution of DEOM-space dynamical observables [48–51],

$$\dot{\hat{\mathbf{A}}}(t) = -i\hat{\mathbf{A}}(t)\mathcal{L}. \quad (24)$$

Here, $\hat{\mathbf{A}} \equiv \{\hat{A}_{\mathbf{n}}^{(n)}\}$ denotes the DEOM-space extension of a conventional dynamical variable \hat{A} , determined via [48–50]

$$\text{Tr}(\hat{A}\rho_T) \equiv \langle\langle\hat{\mathbf{A}}|\rho\rangle\rangle \equiv \sum_{\mathbf{n}} \langle\langle\hat{A}_{\mathbf{n}}^{(n)}|\rho_{\mathbf{n}}^{(n)}\rangle\rangle \equiv \sum_{\mathbf{n}} \text{tr}_S[\hat{A}_{\mathbf{n}}^{(n)}\rho_{\mathbf{n}}^{(n)}].$$

The explicit form of $\{\hat{A}_{\mathbf{n}}^{(n)}\}$ for the dipole operator interested in this work will be presented later; see Eq. (32).

In analogy to $\text{Tr}[\hat{A}(t)\rho_T] = \text{Tr}[\hat{A}\rho_T(t)]$, which dictates the Heisenberg picture in the total composite space, the prescription invariance in the DEOM-space reads as

$$\langle\langle\dot{\hat{\mathbf{A}}}(t)|\rho\rangle\rangle = \langle\langle\hat{\mathbf{A}}|\dot{\rho}(t)\rangle\rangle. \quad (25)$$

This together with Eq. (12), the field-free version, lead to

$$\begin{aligned} \langle\langle\dot{\hat{\mathbf{A}}|\rho\rangle\rangle &= \sum_{\mathbf{n}} \langle\langle\dot{\hat{A}}_{\mathbf{n}}^{(n)}|\rho_{\mathbf{n}}^{(n)}\rangle\rangle \\ &= \sum_{\mathbf{n}} \left\{ -\langle\langle\hat{A}_{\mathbf{n}}^{(n)}|i\mathcal{L}_S + \sum_{ak} n_{ak}\gamma_k|\rho_{\mathbf{n}}^{(n)}\rangle\rangle - i\sum_{ak} \langle\langle\hat{A}_{\mathbf{n}}^{(n)}|\mathcal{A}_a|\rho_{\mathbf{n}_{ak}^+}^{(n+1)}\rangle\rangle \right. \\ &\quad \left. - i\sum_{ak} n_{ak} \langle\langle\hat{A}_{\mathbf{n}}^{(n)}|\mathcal{C}_{ak}|\rho_{\mathbf{n}_{ak}}^{(n-1)}\rangle\rangle \right\}. \end{aligned} \quad (26)$$

The second expression amounts to $\langle\langle\hat{\mathbf{A}}|\dot{\rho}(t)\rangle\rangle$, with Eq. (12) in the absence of external field. By changing the dummy indexes of individual DDOs to all become $|\rho_{\mathbf{n}}^{(n)}\rangle$, we immediately obtain the DEOM in the Heisenberg picture [48–50],

$$\begin{aligned} \dot{\hat{A}}_{\mathbf{n}}^{(n)} &= -\hat{A}_{\mathbf{n}}^{(n)} \left(i\mathcal{L}_S + \sum_{ak} n_{ak}\gamma_k \right) - i\sum_{ak} \hat{A}_{\mathbf{n}_{ak}^+}^{(n-1)} \mathcal{A}_a \\ &\quad - i\sum_{ak} (n_{ak} + 1) \hat{A}_{\mathbf{n}_{ak}^+}^{(n+1)} \mathcal{C}_{ak}. \end{aligned} \quad (27)$$

The involving superoperators in Heisenberg picture read $\hat{\mathcal{O}}\mathcal{L}_S \equiv [\hat{\mathcal{O}}, H_S]$ and

$$\begin{aligned} \hat{\mathcal{O}}\mathcal{A}_a &\equiv [\hat{\mathcal{O}}, \hat{Q}_a], \\ \hat{\mathcal{O}}\mathcal{C}_{ak} &\equiv \sum_b (\eta_{abk} \hat{\mathcal{O}}\hat{Q}_b - \eta_{abk}^* \hat{Q}_b \hat{\mathcal{O}}). \end{aligned} \quad (28)$$

In Eq. (27) \mathcal{A}_a and \mathcal{C}_{ak} act on the $(n \mp 1)$ -level dynamical quantities (Heisenberg picture), whereas in Eq. (12) they are on the $(n \pm 1)$ -level DDOs (Schrödinger picture). The initial values to Eq.

(27), $\{\hat{A}_{\mathbf{n}}^{(n)}(t=0)\} = \{\hat{A}_{\mathbf{n}}^{(n)}\}$, will be discussed later [cf. Eq. (32) and comments there].

Moreover, the derivative-resum scheme, Eq. (14), leads to the terminator in Heisenberg picture,

$$\hat{A}_{\mathbf{n}_{bj}^+}^{(L+1)} = -i\sum_{ak} \hat{A}_{\mathbf{n}_{bjak}^+}^{(L)} \mathcal{A}_a. \quad (29)$$

Apparently, this terminal equation is equivalent to Eq. (14). The proposed derivative-resum scheme does preserve the prescription invariance, without invoking further approximation. It is also numerically most efficient, among all existing truncation schemes we tested by far [37,38,44].

3.2. DEOM-space extension of dynamical variables

The DEOM-space dynamical variable, $\hat{\mathbf{A}} = \{\hat{A}_{\mathbf{n}}^{(n)}\}$, associated to \hat{A} , can be determined uniquely, if \hat{A} can be expressed in terms of the system and/or dissipaton operators. The following procedures of determination are rooted in the fact that the DEOM space is for the dynamics of both the system and the hybrid bath, with the relations of $\text{Tr}[\hat{A}\rho_T(t)] \equiv \langle\langle\hat{\mathbf{A}}|\rho(t)\rangle\rangle$. For a local system operator \hat{A}_S , we have $\hat{\mathbf{A}}_S \equiv \{\hat{A}^{(0)} = \hat{A}_S, \hat{A}_{\mathbf{n}}^{(n>0)} = 0\}$. For a nonlocal \hat{A} involving also dissipatons, the preparation of $\{\hat{A}_{\mathbf{n}}^{(n)}\}$ requires also the generalized Wick's theorem [cf. Eq. (32)]. We exemplify the related issues with the total composite dipole operator in Eq. (3),

$$\hat{V} = \sum_a \mu_a (\hat{\mathbf{X}}_a) \hat{D}_a = \sum_a (\mu_a + v_a \hat{F}_a) \hat{D}_a. \quad (30)$$

Here, $\hat{D}_a = \hat{B}_a^\dagger + \hat{B}_a$ is the system operator, whereas μ_a and v_a are parameters. The hybrid bath operator \hat{F}_a of Eq. (9) is in dissipaton decomposition form. Using the identity $\text{Tr}[\hat{V}\rho_T(t)] = \text{Tr}[\sum_a (\mu_a + v_a \hat{F}_a) \hat{D}_a \rho_T(t)] = \langle\langle\hat{\mathbf{V}}|\rho(t)\rangle\rangle$, we obtain

$$\langle\langle\hat{\mathbf{V}}|\rho(t)\rangle\rangle = \sum_a \left(\mu_a \text{tr}_S[\hat{D}_a \rho_S(t)] + v_a \sum_k \text{tr}_S[\hat{D}_a \rho_{\mathbf{n}_{ak}}^{(1)}(t)] \right). \quad (31)$$

This immediately leads to

$$\hat{\mathbf{V}} = \left\{ \hat{V}^{(0)} = \sum_a \mu_a \hat{D}_a, \hat{V}_{\mathbf{ak}}^{(1)} = v_a \hat{D}_a, \hat{V}_{\mathbf{n}}^{(n>1)} = 0 \right\}. \quad (32)$$

This determines the initial values to DEOM (27) in the Heisenberg picture.

Turn now to the DEOM-space dipole commutator \mathcal{V} , involving in the optical dipole response function,

$$R^{(1)}(t) = i\langle\langle\hat{\mathbf{V}}|\mathcal{G}(t)\mathcal{V}|\rho^{\text{eq}}\rangle\rangle = i\langle\langle\hat{\mathbf{V}}|e^{-i\mathcal{L}t}\mathcal{V}|\rho^{\text{eq}}\rangle\rangle. \quad (33)$$

This is equivalent to the total system-and-bath composite space expression. The DEOM-space dipole commutator reads

$$\mathcal{V}\rho \equiv (\vec{\mathbf{V}} - \vec{\mathbf{V}})\rho. \quad (34)$$

The left-side action along the forward path is evaluated in terms of $\vec{\mathbf{V}}\rho \equiv \vec{\rho} \equiv \{\vec{\rho}_{\mathbf{n}}^{(n)}\}$, where [34–37]

$$\begin{aligned} \vec{\rho}_{\mathbf{n}}^{(n)} &= \text{tr}_B \left[\left(\prod_{bj} \hat{f}_{bj}^{n_{bj}} \right)^\circ \hat{V}\rho_T \right] \\ &= \sum_a \left\{ \mu_a \hat{D}_a \rho_{\mathbf{n}}^{(n)} + v_a \hat{D}_a \sum_k \rho_{\mathbf{n}_{ak}^+}^{(n+1)} + \sum_{bk} n_{ak} \eta_{abk} v_b \hat{D}_b \rho_{\mathbf{n}_{ak}}^{(n-1)} \right\}. \end{aligned} \quad (35)$$

The right-side action along the backward path is evaluated in terms of $\vec{\mathbf{V}}\rho \equiv \vec{\rho} \equiv \{\vec{\rho}_{\mathbf{n}}^{(n)}\}$, where [34–37]

$$\begin{aligned}\bar{\rho}_{\mathbf{n}}^{(n)} &= \text{tr}_B \left[\left(\prod_{bj} \hat{f}_{bj}^{n_{bj}} \right)^\circ \rho_T \hat{V} \right] \\ &= \sum_a \left\{ \mu_a \rho_{\mathbf{n}}^{(n)} \hat{D}_a + v_a \sum_k \rho_{\mathbf{n}_k}^{(n+1)} \hat{D}_a + \sum_{bk} n_{ak} \eta_{abk}^* v_b \rho_{\mathbf{n}_{-k}}^{(n-1)} \hat{D}_b \right\}. \quad (36)\end{aligned}$$

The above three equations identify the DEOM-space dipole commutator action.

3.3. Evaluation of nonlinear optical response functions

In the following, we present an efficient DEOM evaluation of third-order correlation functions, based on the mixed Heisenberg–Schrödinger dynamics scheme, together with block-matrix implementations. Consider the third-order optical response function,

$$R^{(3)}(t_3, t_2, t_1) = i^3 \langle \langle \hat{\mathbf{V}}(t_3) \mathbf{V} \mathbf{G}(t_2) \mathbf{V} \mathbf{G}(t_1) \mathbf{V} | \rho^{\text{eq}} \rangle \rangle. \quad (37)$$

Starting from the equilibrium state ρ^{eq} that is the steady-state solution to the field-free DEOM (23), the evaluation of $R^{(3)}(t_3, t_2, t_1)$ involves sequentially three dipole commutator actions, followed respectively by the t_1 -, t_2 - and t_3 -propagations. The above protocol is the Schrödinger dynamics prescription, with all three temporal evolutions on the DEOM-space state vectors. Alternatively, we implement the t_3 -propagation in the Heisenberg picture, in parallel with the t_1 - and t_2 -propagations in the Schrödinger picture. We evaluate $\hat{\mathbf{V}}(t_3) \equiv \hat{\mathbf{V}} \mathbf{G}(t_3)$ by integrating Eq. (24), with the initial $\hat{\mathbf{V}}(0) = \hat{\mathbf{V}}$ of Eq. (32). We then recast Eq. (37) into

$$R^{(3)}(t_3, t_2, t_1) = i^3 \langle \langle \hat{\mathbf{V}}(t_3) | \mathbf{V} \mathbf{G}(t_2) \mathbf{V} \mathbf{G}(t_1) \mathbf{V} | \rho^{\text{eq}} \rangle \rangle. \quad (38)$$

Apparently, the mixed Heisenberg–Schrödinger scheme facilitates the evaluation of third-order response functions. In fact, this scheme is closely related to the doorway/window picture of pump–probe spectroscopy [52].

The third-order response function of Eq. (38) can be expanded to eight Liouville-space pathway components and their complex conjugate counterparts, resulting in [47,48,53]

$$R^{(3)}(t_3, t_2, t_1) = i^3 \sum_{\alpha=1}^8 [R_\alpha(t_3, t_2, t_1) - \text{c.c.}]. \quad (39)$$

The involving eight pathway components are related to the double-sided Feynman diagrams in Fig. 1, and can be arranged into block-matrix form, as follows [48].

$$\begin{aligned}R_1 &= \langle \langle \hat{\mathbf{V}}_{ge}(t_3) | \bar{\mathbf{V}}_{eg} \mathcal{G}_{ee}(t_2) \bar{\mathbf{V}}_{eg} \mathcal{G}_{eg}(t_1) \bar{\mathbf{V}}_{eg} | \rho_{gg}^{\text{eq}} \rangle \rangle, \\ R_2 &= \langle \langle \hat{\mathbf{V}}_{ge}(t_3) | \bar{\mathbf{V}}_{eg} \mathcal{G}_{ee}(t_2) \bar{\mathbf{V}}_{eg} \mathcal{G}_{ge}(t_1) \bar{\mathbf{V}}_{ge} | \rho_{gg}^{\text{eq}} \rangle \rangle, \\ R_3 &= \langle \langle \hat{\mathbf{V}}_{ge}(t_3) | \bar{\mathbf{V}}_{eg} \mathcal{G}_{gg}(t_2) \bar{\mathbf{V}}_{eg} \mathcal{G}_{ge}(t_1) \bar{\mathbf{V}}_{ge} | \rho_{gg}^{\text{eq}} \rangle \rangle, \\ R_4 &= \langle \langle \hat{\mathbf{V}}_{ge}(t_3) | \bar{\mathbf{V}}_{eg} \mathcal{G}_{gg}(t_2) \bar{\mathbf{V}}_{ge} \mathcal{G}_{eg}(t_1) \bar{\mathbf{V}}_{eg} | \rho_{gg}^{\text{eq}} \rangle \rangle, \\ R_5 &= -\langle \langle \hat{\mathbf{V}}_{ef}(t_3) | \bar{\mathbf{V}}_{fe} \mathcal{G}_{ee}(t_2) \bar{\mathbf{V}}_{eg} \mathcal{G}_{ge}(t_1) \bar{\mathbf{V}}_{ge} | \rho_{gg}^{\text{eq}} \rangle \rangle, \\ R_6 &= -\langle \langle \hat{\mathbf{V}}_{ef}(t_3) | \bar{\mathbf{V}}_{fe} \mathcal{G}_{ee}(t_2) \bar{\mathbf{V}}_{ge} \mathcal{G}_{eg}(t_1) \bar{\mathbf{V}}_{eg} | \rho_{gg}^{\text{eq}} \rangle \rangle, \\ R_7 &= -\langle \langle \hat{\mathbf{V}}_{ef}(t_3) | \bar{\mathbf{V}}_{ge} \mathcal{G}_{fg}(t_2) \bar{\mathbf{V}}_{fe} \mathcal{G}_{eg}(t_1) \bar{\mathbf{V}}_{eg} | \rho_{gg}^{\text{eq}} \rangle \rangle, \\ R_8 &= \langle \langle \hat{\mathbf{V}}_{ge}(t_3) | \bar{\mathbf{V}}_{ef} \mathcal{G}_{fg}(t_2) \bar{\mathbf{V}}_{fe} \mathcal{G}_{eg}(t_1) \bar{\mathbf{V}}_{eg} | \rho_{gg}^{\text{eq}} \rangle \rangle.\end{aligned} \quad (40)$$

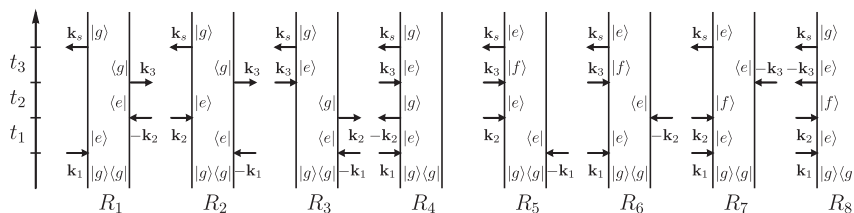


Fig. 1. Double-sided Feynman diagrams for two-dimensional spectroscopy in the rotating wave approximation. The ket and bra notations specify the Liouville-space pathways evolving in the t_1 -, t_2 - and t_3 -delay time intervals.

The block-matrix DEOM dynamics involves three manifolds of electronic state [48,54], the ground $|g\rangle$, the singly-excited $|e\rangle \equiv \sum_a \hat{B}_a^\dagger |g\rangle$, and the doubly-excited $|f\rangle \equiv \sum_{a>b} \hat{B}_a^\dagger \hat{B}_b^\dagger |g\rangle$. For an M -chromophore system, this three electronic manifolds have the dimensions of $N_g = 1$, $N_e = M$ and $N_f = M(M-1)/2$, respectively. In the adiabatic limit, the relaxation occurs only within electronic manifolds, while the inter-manifold transitions are mediated by the optical dipole operator. This is the case we consider here. While the electronic transition dipole operators $\{\hat{D}_a\}$ are non-diagonal, both system Hamiltonian H_S and dissipative modes $\{\hat{Q}_a\}$, which dictate the field-free DEOM propagator, are block diagonalized. Consequently, both the DEOM-space extension of dynamical variables and the state vectors are in the block form, see Eq. (40). To proceed, we denote

$$\rho_{uv} \equiv \left\{ \rho_{\mathbf{n};uv}^{(n)} \right\} \equiv \left\{ |u\rangle \langle u| \rho_{\mathbf{n}}^{(n)} |v\rangle \langle v| \right\},$$

with $\rho_{\mathbf{n};vu}^{(n)} = \rho_{\mathbf{n};uv}^{(n)\dagger}$, where $(u, v) \in \{g, e, f\}$. Each $\rho_{\mathbf{n};uv}^{(n)}$ is an $N_u \times N_v$ matrix. Similarly,

$$\hat{\mathbf{A}}_{vu} \equiv \left\{ \hat{A}_{\mathbf{n};vu}^{(n)} \right\} \equiv \left\{ |v\rangle \langle v| \hat{A}_{\mathbf{n}}^{(n)} |u\rangle \langle u| \right\},$$

for the DEOM-space dynamical variables. Since DEOM recovers HEOM in absence of the bath-induced non-Condon polarization, the equations of motion for field-free $\{\rho_{\mathbf{n};uv}^{(n)}\}$ or those for $\{\hat{A}_{\mathbf{n};vu}^{(n)}\}$ are the same as the block HEOM formalism; see Ref. [48].

4. Numerical demonstrations

4.1. Solvent-induced non-Condon polarization

For demonstration on the solvent-induced non-Condon polarization dynamics, we set the excitation laser field the following form,

$$\mu_T \varepsilon(t) = \frac{\theta}{\sqrt{2\pi}\sigma} \exp\left(-\frac{t^2}{2\sigma^2}\right) \cos(\omega_c t). \quad (41)$$

Here, θ , σ and ω_c are the flipping angle, temporal variance and carrier frequency, respectively. The total dipole strength assumes $\mu_T = \mu + |\mu'|$, with the Condon part $\mu \geq 0$ and the non-Condon $\mu' \equiv 2\lambda v$ that arises from bath induced polarization and can be any sign. We set $J_{ab}(\omega) = \delta_{ab} J(\omega)$, with

$$J(\omega) = \frac{2\lambda\gamma\omega}{\omega^2 + \gamma^2}. \quad (42)$$

Here, λ and γ are the exciton–phonon coupling strength and bath cutoff frequency.

In this subsection, we demonstrate the solvent-induced non-Condon polarization and Fano interference with an excitonic monomer. The transition dipole of the monomer is $\hat{V} = (\mu + v\hat{F})\hat{D} = [\mu + \mu'/(2\lambda)\hat{F}]\hat{D}$. Three representing values of $\mu'/\mu_T = 0, 0.5$, and 1 are used in demonstrations, covering from the Condon limit, to the case of $\mu = 0$. The adopted field strengths are $\theta = 0.01\pi, 0.5\pi$, and π , from weak to strong. Fig. 2 presents the

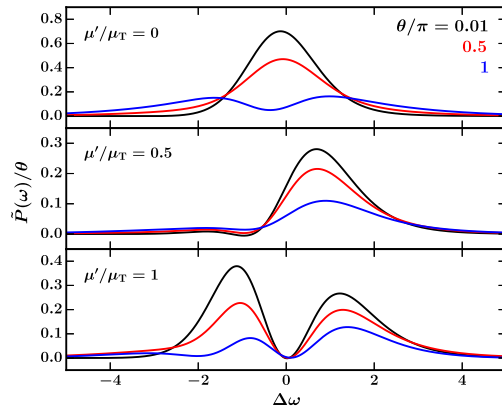


Fig. 2. Field-dressed polarization spectrum of an excitonic monomer, with $\mu'/\mu_T = 0$ (top), 0.5 (middle) and 1 (bottom) for the transition dipole element specified in the main text. $\Delta\omega = \omega - \epsilon$ and given in unit of $k_B T \equiv 1/\beta$. The excitation fields are resonant with the excitonic monomer, with $\beta\omega_c = \beta\epsilon = 10$ and $\sigma = 0.5\beta$, for all three strengths, $\theta = 0.01\pi$ (black), 0.5π (red) and π (blue). The bath spectral density adopts the Drude model with $\beta\lambda = \beta\gamma = 0.5$. (For interpretation of the references to color in this figure legend, the reader is referred to the web version of this article.)

resulting polarization spectrum, $\tilde{P}(\omega) = \text{Im} \int dt e^{i\omega t} [P(t) - P_{\text{eq}}]$, where [cf. Eq. (31)]

$$P(t) = \text{Tr}[\hat{V}\rho_T(t)] = \mu \text{tr}_S[\hat{D}\rho^{(0)}(t)] + v \sum_k \text{tr}_S[\hat{D}\rho_k^{(1)}(t)].$$

The simulated polarization spectra demonstrate both the strong field nonlinear effect and the solvent-induced non-Condon polarization. As anticipated, with the increase of the field strength in each panel, we find the spectrum bleaching around $\omega = \epsilon$ [55–57]. On the other hand, with the increase of $\mu'/\mu_T = 2\lambda v/(\mu + 2\lambda|v|)$ from the top panel to the bottom one, the resonant peak splits into two non-Condon bands, with the blue-side one emerges first for $v > 0$, but the red-band could become overwhelming, when the Condon part (μ) decreases and in the weak excitation regime. As the non-Condon effect in study arises purely from the solvent polarization that accompanies with the electronic transition, the observed features in Fig. 2 would represent a type of Fano interference between the solvent continuum and the system discrete. The detailed features result from the interplay between the excitation field, the strength of Condon transition versus that of the solvent-induced non-Condon transition, and its relative sign with respect the former.

We further illustrate the excitation entanglement between system and solvation bath, by considering the linear absorption spectrum. The results reported in Fig. 3 are evaluated via [cf. Eqs. (33) and (34)]

$$\begin{aligned} S(\omega) &= \text{Re} \int_0^\infty dt e^{i\omega t} \text{Tr}[\hat{V} e^{-i\mathcal{L}_T t} \hat{V} \rho_T^{\text{eq}}] \\ &= \text{Re} \int_0^\infty dt e^{i\omega t} \langle \hat{V} | e^{-i\mathcal{L}t} \hat{V} | \rho^{\text{eq}} \rangle. \end{aligned} \quad (43)$$

The Fano turnover features are observed again, with the bath-induced non-Condon two-bands, where the red-side band emerges first when $v < 0$ and vice versa. In fact, we have $S(\omega) = (1 - e^{\beta\omega})^{-1} [\text{Im} \tilde{P}(\omega)/\tilde{E}(\omega)]_{\theta \rightarrow 0}$. This identity indicates that the linear spectrum can also be evaluated via the field-dressed DEOM dynamics approach, as we did for Fig. 2. We have verified that the above two approaches give the same numerical results in the linear response regime. Moreover, for a two-level system as studied here, the linear absorption profile can be obtained analytically, resulting in $S(\omega) = (\mu + v\Delta\omega)^2 S_0(\omega)$, where

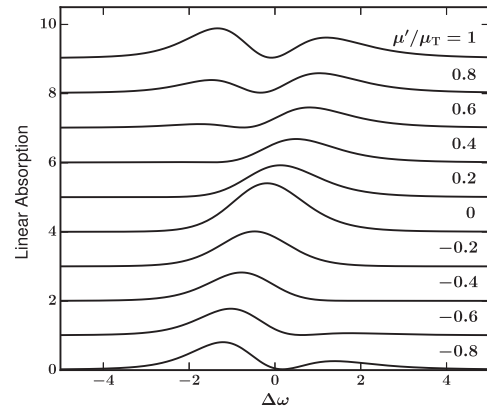


Fig. 3. Linear absorption lineshapes for the excitonic monomer of Fig. 2, with selected μ'/μ_T ranging from -0.8 to 1 . For clearness, we have cumulatively lifted up the baselines of all curves by 1 unit.

$S_0(\omega) = \text{Re} \int_0^\infty dt e^{i\Delta\omega t - g(t)}$ denotes the result in the Condon limit, with $g(t)$ being the well-known lineshape function for the simple two-level system [47,53]. The DEOM evaluation results reported in Fig. 3 agree completely with the analytical expression.

4.2. Two-dimensional coherent spectroscopy

Two-dimensional coherent spectroscopy is a four-wave-mixing technique [47]. In experiment, the sample is excited by three time-ordered laser pulses (with wavevectors $\mathbf{k}_1, \mathbf{k}_2$ and \mathbf{k}_3) separated by time interval t_1 and t_2 , and after a time-delay t_3 , the emitted signal is measured along the phase matching direction $\mathbf{k}_s = \pm\mathbf{k}_3 \pm \mathbf{k}_2 \pm \mathbf{k}_1$. The $S_{\mathbf{k}_i}$ signal goes with $\mathbf{k}_s = \mathbf{k}_3 + \mathbf{k}_2 - \mathbf{k}_1$, that is the stimulated photon echo or rephasing configuration [58]. The non-rephasing $S_{\mathbf{k}_{ii}}$ signal is with $\mathbf{k}_s = \mathbf{k}_3 - \mathbf{k}_2 + \mathbf{k}_1$. The $S_{\mathbf{k}_{iii}}$ signal goes with $\mathbf{k}_s = -\mathbf{k}_3 + \mathbf{k}_2 + \mathbf{k}_1$, which is the double-excitation configuration [59], involving the R_7 and R_8 pathways in the double-sided Feynman diagrams in Fig. 1.

Experiments can also be performed in the configuration that the pulsed \mathbf{k}_2 -field is applied continuously not only after but also before the \mathbf{k}_1 -field [17,18,48]. The resulting signal amounts to $S_{\mathbf{k}_i + \mathbf{k}_{ii}} = S_{\mathbf{k}_i} + S_{\mathbf{k}_{ii}}$. The pump-probe absorption configuration [47,52], involves all the six pathways from R_1 to R_6 . In the $S_{\mathbf{k}_{i/ii}}$ and pump-probe configurations, the t_1 and t_3 represent the excitation and detection time intervals, and therefore, the ω_1 and ω_3 in Eq. (44) are the excitation and detection frequencies, respectively. The t_2 denotes the waiting time, during which the system evolves in either the excited or the ground state manifold, with underlying dynamics being governed by $\mathcal{G}_{ee}(t_2)$ or $\mathcal{G}_{gg}(t_2)$, respectively; see Eq. (40). The efficient DEOM evaluations on $R_x(t_3, t_2, t_1)$ had been detailed in Section 3.3.

For simplicity, we adopt the rotating wave approximation and the impulsive limit [47]. With the aid of the double-sided Feynman diagrams in Fig. 1, the $S_{\mathbf{k}_{i/ii}}$ signal is given by [17,18,48]

$$\begin{aligned} S_{\mathbf{k}_{i/ii}}(\omega_3, t_2, \omega_1) &= \text{Re} \int_0^\infty dt_3 \int_0^\infty dt_1 e^{i(\Delta\omega_3 t_3 \mp \Delta\omega_1 t_1)} \\ &\quad \times R_{\mathbf{k}_{i/ii}}(t_3, t_2, t_1), \end{aligned} \quad (44)$$

where $\Delta\omega_k = \omega_k - \epsilon$, and

$$\begin{aligned} R_{\mathbf{k}_i} &= R_2 + R_3 + R_5 \quad (\text{rephasing}), \\ R_{\mathbf{k}_{ii}} &= R_1 + R_4 + R_6 \quad (\text{non-rephasing}). \end{aligned} \quad (45)$$

We illustrate the non-Condon solvent polarization effect on $S_{\mathbf{k}_i}(\omega_3, t_2 = 0, \omega_1)$ and $S_{\mathbf{k}_{ii}}(\omega_3, t_2 = 0, \omega_1)$. Fig. 4 depicts the results for the three representing excitonic monomers of Fig. 2.

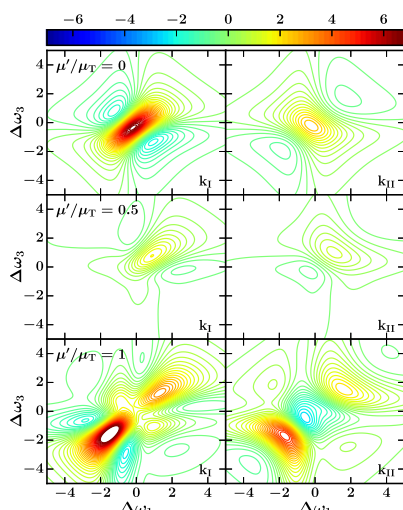


Fig. 4. Coherent two-dimensional spectroscopy, $S_{k_l/k_{ll}}(\omega_3, 0, \omega_1)$, for the excitonic monomer of Fig. 2.

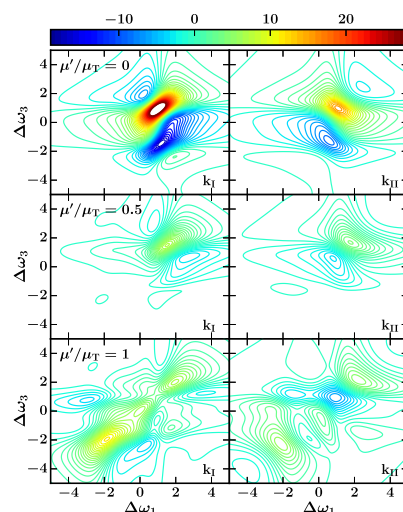


Fig. 5. Coherent two-dimensional spectroscopy, $S_{k_l/k_{ll}}(\omega_3, 0, \omega_1)$, for an excitonic homo-dimer. We set $\beta V_{12} = 1$ and $\beta U_{12} = 0$ and $\mu'/\mu_T = \mu'_1/\mu_T = \mu'_2/\mu_T = 0$ (top), 0.5 (middle) and 1 (bottom).

While the top panels are for the Condon transition limit ($\mu'/\mu = 0$), the middle panels are for the intermediate non-Condon strength with $\mu'/\mu = 1$, whereas the bottom ones are for the pure non-Condon limit ($\mu = 0$). The diagonal profiles of the two-dimensional spectroscopies reproduce the basic features of Fig. 3 about the development of two-band features, as the strength of non-Condon transition increases. The anti-diagonal features, however, experience suppression (middle-panels), and then prominent interference (bottom-panels). Let us examine the \mathbf{k}_l -signal in the pure non-Condon limit (the bottom-left panel of Fig. 4), versus its pure Condon limit counterpart (the top-left panel of Fig. 4). The diagonal elongation splits into two bands, where the resonant peak around $\Delta\omega = 0$ is diminished and the red-band becomes dominant. Similar results are found when comparing the non-Condon \mathbf{k}_{ll} -signal to the Condon counterpart. The interference is strengthened by the strong negative dip around $\Delta\omega = 0$ and the strengthening of the red-band, see the bottom-right panel of Fig. 4.

In Fig. 5, we present the results for a homo-dimer system, with $\beta V_{12} = 1$ and $\beta U_{12} = 0$. The top panels that correspond to the Condon transition limit show clearly the interference between two excitons. The basic feature there can be explained via the molecu-

lar aggregate excitonic dipole symmetry analysis [48]. This excitonic interference is concealed as the strength of the non-Condon transition increases. For intermediate non-Condon strength with $\mu'/\mu = 1$, the dimer results (middle panels of Fig. 5) are very similar to the monomer cases (middle panels of Fig. 4). In the pure non-Condon case ($\mu = 0$), the correlated system-and-bath interference becomes much more complicated, see bottom panels of Fig. 5. Related analysis will be scrutinized elsewhere.

5. Concluding remarks

We have comprehensively reviewed the DEOM theory [34–37], in contact with the solvent-induced non-Condon polarization, followed by demonstrations on this novel type of Fano interference spectroscopies, both linear and nonlinear. Evidently, the DEOM theory is capable of studying hybrid bath dynamics, as supported by the fact that it reproduces the analytical results of the linear absorption with non-Condon solvent excitation, see the discussion to the end of Section 4.1. The DEOM theory is not only about Eq. (12) for the time evolution of the involving DDOs, but more importantly on the underlying dissipaton algebra detailed in Section 2.3 and Section 3. Important ingredients for hybrid bath dynamics include also the generalized Wick's theorem and the DEOM-space extension of dynamical operators and their commutator actions. The advanced technique is also about the derivative-resum level truncation scheme, Eqs. (14) and (15), which is numerically efficient and preserves the prescription invariance. The resulting DEOM thus supports the mixed Heisenberg–Schrödinger dynamics for efficient evaluation of nonlinear response functions.

Note that the linear absorption with non-Condon solvent excitation discussed in Section 4.1 is a novel type of Fano profile spectroscopy. It is originated from the optical response interference between discrete electronic transition and the non-Condon solvent continuum polarization. The analytical solution is $S(\omega) = (\mu + \nu\Delta\omega)^2 S_0(\omega)$, where $S_0(\omega)$ denotes the result in the Condon limit. The conventional Fano profile is recovered when $S_0(\omega)$ is in Lorentz line shape [60]. In our previous study on the Fano interference in Brownian oscillator systems, the DEOM evaluations also reproduce the analytical results there [61]. The DEOM theory, including the underlying dissipaton algebra, does serve a versatile means for an accurate evaluation of system and hybrid bath dynamics in various scenarios.

Acknowledgements

The support from the National Natural Science Foundation of China (Nos. 21373191, 21303175, 21322305, and 21233007) is gratefully acknowledged.

References

- [1] P. Hänggi, P. Talkner, M. Borkovec, Reaction-rate theory: fifty years after Kramers, *Rev. Mod. Phys.* 62 (1990) 251–341.
- [2] S. Datta, *Quantum Transport: Atom to Transistor*, Cambridge University Press, New York, 2005.
- [3] Y.C. Cheng, G.R. Fleming, Dynamics of light harvesting in photosynthesis, *Annu. Rev. Phys. Chem.* 60 (2009) 241–262.
- [4] Y. Tanimura, R. Kubo, Time evolution of a quantum system in contact with a nearly Gaussian–Markovian noise bath, *J. Phys. Soc. Jpn* 58 (1989) 101–114.
- [5] Y.A. Yan, F. Yang, Y. Liu, J.S. Shao, Hierarchical approach based on stochastic decoupling to dissipative systems, *Chem. Phys. Lett.* 395 (2004) 216–221.
- [6] Y. Tanimura, Nonperturbative expansion method for a quantum system coupled to a harmonic-oscillator bath, *Phys. Rev. A* 41 (1990) 6676–6687.
- [7] Y. Tanimura, Stochastic Liouville, Langevin, Fokker–Planck, and master equation approaches to quantum dissipative systems, *J. Phys. Soc. Jpn* 75 (2006) 082001.
- [8] A. Ishizaki, Y. Tanimura, Quantum dynamics of system strongly coupled to low temperature colored noise bath: reduced hierarchy equations approach, *J. Phys. Soc. Jpn* 74 (2005) 3131–3134.

- [9] Y. Tanimura, Reduced hierarchical equations of motion in real and imaginary time: correlated initial states and thermodynamic quantities, *J. Chem. Phys.* 141 (2014). 044114.
- [10] Y. Tanimura, Real-time and imaginary-time quantum hierarchal Fokker–Planck equations, *J. Chem. Phys.* 142 (2015). 144110.
- [11] R.X. Xu, P. Cui, X.Q. Li, Y. Mo, Y.J. Yan, Exact quantum master equation via the calculus on path integrals, *J. Chem. Phys.* 122 (2005). 041103.
- [12] R.X. Xu, Y.J. Yan, Dynamics of quantum dissipation systems interacting with bosonic canonical bath: hierarchical equations of motion approach, *Phys. Rev. E* 75 (2007). 031107.
- [13] X. Zheng, R.X. Xu, J. Xu, J.S. Jin, J. Hu, Y.J. Yan, Hierarchical equations of motion for quantum dissipation and quantum transport, *Prog. Chem.* 24 (2012) 1129–1152. <http://www.progchem.ac.cn/EN/abstract/abstract10858.shtml>.
- [14] J.S. Jin, X. Zheng, Y.J. Yan, Exact dynamics of dissipative electronic systems and quantum transport: hierarchical equations of motion approach, *J. Chem. Phys.* 128 (2008). 234703.
- [15] Z.H. Li, N.H. Tong, X. Zheng, D. Hou, J.H. Wei, J. Hu, Y.J. Yan, Hierarchical Liouville-space approach for accurate and universal characterization of quantum impurity systems, *Phys. Rev. Lett.* 109 (2012). 266403.
- [16] V. Chernyak, W.M. Zhang, S. Mukamel, Multidimensional femtosecond spectroscopies of molecular aggregates and semiconductor nanostructures: the nonlinear exciton equations, *J. Chem. Phys.* 109 (1998) 9587–9601.
- [17] S. Mukamel, D. Abramavicius, Many-body approaches for simulating coherent nonlinear spectroscopies of electronic and vibrational excitons, *Chem. Rev.* 104 (2004) 2073–2098.
- [18] S. Mukamel, Y. Tanimura, P. Hamm, Coherent multidimensional optical spectroscopy, *Special Issue of Acc. Chem. Res.* 42 (2009) 1207–1469.
- [19] G.S. Engel, T.R. Calhoun, E.L. Read, T.K. Ahn, T. Mančal, Y.C. Cheng, R.E. Blankenship, G.R. Fleming, Evidence for wavelike energy transfer through quantum coherence in photosynthetic systems, *Nature* 446 (2007) 782–786.
- [20] Y.C. Cheng, G.R. Fleming, Coherence quantum beats in two-dimensional electronic spectroscopy, *J. Phys. Chem. B* 112 (2008) 4254–4260.
- [21] G. Panitchayangkoon, D. Hayes, K.A. Fransted, J.R. Caram, E. Harel, J. Wen, R.E. Blankenship, G.S. Engel, Long-lived quantum coherence in photosynthetic complexes at physiological temperature, *Proc. Natl. Acad. Sci. USA* 107 (2010) 12766–12770.
- [22] M.B. Plenio, J. Almeida, S.F. Huelga, Origin of long-lived oscillations in 2D-spectra of a quantum vibronic model: electronic versus vibrational coherence, *J. Chem. Phys.* 139 (2013). 235102.
- [23] R. Tempelaar, T.L.C. Jansen, J. Knoester, Vibrational beatings conceal evidence of electronic coherence in the FMO light-harvesting complex, *J. Phys. Chem. B* 118 (2014) 12865–12872.
- [24] Y. Fujihashi, G.R. Fleming, A. Ishizaki, Impact of environmentally induced fluctuations on quantum mechanically mixed electronic and vibrational pigment states in photosynthetic energy transfer and 2D electronic spectra, *J. Chem. Phys.* 142 (2015). 212403.
- [25] D.M. Monahan, L. Whaley-Mayda, A. Ishizaki, G.R. Fleming, Influence of weak vibrational-electronic couplings on 2D electronic spectra and inter-site coherence in weakly coupled photosynthetic complexes, *J. Chem. Phys.* 143 (2015). 065101.
- [26] Y. Tanimura, S. Mukamel, Optical Stark spectroscopy of a Brownian oscillator in intense fields, *J. Phys. Soc. Jpn* 63 (1994) 66–77.
- [27] Y. Tanimura, Y. Maruyama, Gaussian–Markovian quantum Fokker–Planck approach to nonlinear spectroscopy of a displaced Morse potentials system: dissociation, predissociation, and optical Stark effects, *J. Chem. Phys.* 107 (1997) 1779–1793.
- [28] Y. Tanimura, T. Steffen, Two-dimensional spectroscopy for harmonic vibrational modes with nonlinear system-bath interactions. II. Gaussian–Markovian case, *J. Phys. Soc. Jpn* 69 (2000) 4095–4106.
- [29] T. Kato, Y. Tanimura, Two-dimensional Raman and infrared vibrational spectroscopy for a harmonic oscillator system nonlinearly coupled with a colored noise bath, *J. Chem. Phys.* 120 (2004) 260–271.
- [30] A. Ishizaki, G.R. Fleming, On the adequacy of the Redfield equation and related approaches to the study of quantum dynamics in electronic energy transfer, *J. Chem. Phys.* 130 (2009). 234110.
- [31] A. Ishizaki, G.R. Fleming, Unified treatment of quantum coherent and incoherent hopping dynamics in electronic energy transfer: reduced hierarchy equation approach, *J. Chem. Phys.* 130 (2009). 234111.
- [32] L.P. Chen, R.H. Zheng, Q. Shi, Y.J. Yan, Optical line shapes of molecular aggregates: hierarchical equations of motion method, *J. Chem. Phys.* 131 (2009). 094502.
- [33] L.P. Chen, R.H. Zheng, Y.Y. Jing, Q. Shi, Simulation of the two-dimensional electronic spectra of the Fenna–Matthews–Olson complex using the hierarchical equations of motion method, *J. Chem. Phys.* 134 (2011). 194508.
- [34] Y.J. Yan, Theory of open quantum systems with bath of electrons and phonons and spins: Many-dissipation density matrixes approach, *J. Chem. Phys.* 140 (2014). 054105.
- [35] H.D. Zhang, R.X. Xu, X. Zheng, Y.J. Yan, Nonperturbative spin-boson and spin-spin dynamics and nonlinear Fano interferences: a unified dissipation theory based study, *J. Chem. Phys.* 142 (2015). 024112.
- [36] J.S. Jin, S.K. Wang, X. Zheng, Y.J. Yan, Current noise spectra and mechanisms with dissipation equation of motion theory, *J. Chem. Phys.* 142 (2015). 234108.
- [37] Y.J. Yan, J.S. Jin, R.X. Xu, X. Zheng, Dissipation equation of motion approach to open quantum systems, *Front. Phys.* 11 (2016) 110306, <http://dx.doi.org/10.1007/s11467-016-0513-5>.
- [38] H.D. Zhang, Y.J. Yan, Onsets of hierarchy truncation and self-consistent Born approximation with quantum mechanics prescriptions invariance, *J. Chem. Phys.* 143 (2015). 214112.
- [39] U. Weiss, *Quantum Dissipative Systems*, Series in Modern Condensed Matter Physics, third ed., vol. 13, World Scientific, Singapore, 2008.
- [40] Y.J. Yan, R.X. Xu, Quantum mechanics of dissipative systems, *Annu. Rev. Phys. Chem.* 56 (2005) 187–219.
- [41] J.J. Ding, J. Xu, J. Hu, R.X. Xu, Y.J. Yan, Optimized hierarchical equations of motion for Drude dissipation with applications to linear and nonlinear optical responses, *J. Chem. Phys.* 135 (2011). 164107.
- [42] J.J. Ding, R.X. Xu, Y.J. Yan, Optimizing hierarchical equations of motion for quantum dissipation and quantifying quantum bath effects on quantum transfer mechanisms, *J. Chem. Phys.* 136 (2012). 224103.
- [43] R.P. Feynman, F.L. Vernon Jr., The theory of a general quantum system interacting with a linear dissipative system, *Ann. Phys.* 24 (1963) 118–173.
- [44] D. Hou, S.K. Wang, R.L. Wang, L.Z. Ye, R.X. Xu, X. Zheng, Y.J. Yan, Improving the efficiency of hierarchical equations of motion approach and application to coherent dynamics in Aharonov–Bohm interferometers, *J. Chem. Phys.* 142 (2015). 104112.
- [45] Y. Tanimura, P.G. Wolynes, Quantum and classical Fokker–Planck equations for a Gaussian–Markovian noise bath, *Phys. Rev. A* 43 (1991) 4131–4142.
- [46] Y. Tanimura, P.G. Wolynes, The interplay of tunneling, resonance, and dissipation in quantum barrier crossing: a numerical study, *J. Chem. Phys.* 96 (1992) 8485–8496.
- [47] S. Mukamel, *The Principles of Nonlinear Optical Spectroscopy*, Oxford University Press, New York, 1995.
- [48] J. Xu, R.X. Xu, D. Abramavicius, H.D. Zhang, Y.J. Yan, Advancing hierarchical equations of motion for efficient evaluation of coherent two-dimensional spectroscopy, *Chin. J. Chem. Phys.* 24 (2011) 497–506.
- [49] K.B. Zhu, R.X. Xu, H.Y. Zhang, J. Hu, Y.J. Yan, Hierarchical dynamics of correlated system–environment coherence and optical spectroscopy, *J. Phys. Chem. B* 115 (2011) 5678–5684.
- [50] J. Xu, H.D. Zhang, R.X. Xu, Y.J. Yan, Correlated driving and dissipation in two-dimensional spectroscopy, *J. Chem. Phys.* 138 (2013). 024106.
- [51] Y. Mo, R.X. Xu, P. Cui, Y.J. Yan, Correlation and response functions with non-Markovian dissipation: a reduced Liouville-space theory, *J. Chem. Phys.* 122 (2005). 084115.
- [52] Y.J. Yan, S. Mukamel, Femtosecond pump-probe spectroscopy of polyatomic molecules in condensed phases, *Phys. Rev. A* 41 (1990) 6485–6505.
- [53] Y.J. Yan, S. Mukamel, Electronic dephasing, vibrational relaxation, and solvent friction in molecular nonlinear optical lineshapes, *J. Chem. Phys.* 89 (1988) 5160–5176.
- [54] D. Abramavicius, B. Palmieri, D.V. Voronine, F. Šanda, S. Mukamel, Coherent multidimensional optical spectroscopy of excitons in molecular aggregates; quasiparticle versus supermolecule perspectives, *Chem. Rev.* 109 (2009) 2350–2408.
- [55] A.E. Siegman, *Lasers*, University Science Books, 1986.
- [56] L. Allen, J.H. Eberly, *Optical Resonance and Two-Level Atoms*, Dover, New York, 1987.
- [57] J. Adolphs, M. Berr, T. Renger, Hole-burning spectroscopy on excitonically coupled pigments in proteins: theory meets experiment, *J. Am. Chem. Soc.* 138 (2016) 2993–3001.
- [58] Y.J. Yan, S. Mukamel, Photon echoes of polyatomic molecules in condensed phases, *J. Chem. Phys.* 94 (1991) 179–190.
- [59] S. Mukamel, R. Oszwaldowski, L. Yang, A coherent nonlinear optical signal induced by electron correlations, *J. Chem. Phys.* 127 (2007). 221105.
- [60] U. Fano, Effects of configuration interaction on intensities and phase shifts, *Phys. Rev.* 124 (1961). 1866.
- [61] R.X. Xu, H.D. Zhang, X. Zheng, Y.J. Yan, Dissipation equation of motion for system-and-bath interference dynamics, *Sci. China Chem.* 58 (2015) 1816–1824. Special Issue: Lemin Li Festschrift.